This is a repository copy of *In situ TiC reinforced Ti6Al4V matrix composites manufactured via selective laser melting*.

White Rose Research Online URL for this paper:
https://eprints.whiterose.ac.uk/208349/

Version: Accepted Version

In situ TiC Reinforced Ti6Al4V Matrix Composites Manufactured via Selective Laser Melting

İdris Tuğrul Gülenç[1,3*], Mingwen Bai[2], Ria L. Mitchell[1], Iain Todd[1], Beverley J Inkson[1*]

[1] Department of Materials Science and Engineering, The University of Sheffield, S1 3JD, Sheffield, UK
[2] School of Mechanical Engineering, Leeds University, LS2 9JT, Leeds, UK
[3] Department of Metallurgical and Materials Engineering, Ankara Yildirim Beyazit University, Turkey
[*] Corresponding authors, email: idristugrul.gulenc@aybu.edu.tr, beverley.inkson@sheffield.ac.uk

Abstract

Purpose – Current methods for the preparation of composite powder feedstock for selective laser melting rely on costly nanoparticles or yield inconsistent powder morphology. This study aims to develop a cost-effective Ti6Al4V-carbon feedstock, which preserves the parent Ti6Al4V particle's flowability, and produces in situ TiC reinforced Ti6Al4V composites with superior traits.

Design/method/approach – Ti6Al4V particles were directly mixed with graphite flakes in a planetary ball mill. This composite powder feedstock was used to manufacture in situ TiC-Ti6Al4V composites using various energy densities. Relative porosity, microstructure, and hardness of the composites were evaluated for different SLM processing parameters.

Findings – Homogeneously carbon coated Ti6Al4V particles were produced by direct mixing. After SLM processing, *in situ* grown 100-500 nm size TiC nanoparticles were distributed within the α-martensite Ti6Al4V matrix. The formation of TiC particles refines the Ti6Al4V β grain size. Relative density varied between 96.4%-99.5% depending on the processing parameters. Hatch distance, exposure time and point distance were all effective on relative porosity change whereas only exposure time and point distance were effective on hardness change.

Originality/value – This work introduces a novel, cost-effective powder feedstock preparation method for selective laser melting manufacture of Ti6Al4V-TiC composites. The in situ SLM composites achieved in this study have high relative density values, well dispersed TiC nanoparticles, and increased hardness. Additionally, the feedstock preparation method can be readily adapted for various matrix and reinforcement materials in future studies.

Keywords: selective laser melting, TiC, Ti6Al4V, in situ, TMCs

---

[1] Department of Materials Science and Engineering, The University of Sheffield, S1 3JD, Sheffield, UK
[2] Institute for Clean Growth and Future Mobility, Coventry University, CV1 5FB, Coventry, UK
[*] Corresponding authors, email: i.t.gulenc@sheffield.ac.uk, beverley.inkson@sheffield.ac.uk

1 Introduction

Titanium alloys are extensively used in military, aerospace, power generation, marine, sports, and transportation industries because of their high strength to weight ratio and corrosion resistance (Donachie, 2000a; Peters *et al.*, 2005). This strength allows component weight reductions without a trade-off for mechanical properties. Ti-6Al-4V alloy (or Ti6Al4V) is the most widely used titanium alloy (Donachie, 2000b) and also one of the most studied alloys for additive manufacturing (AM) (DebRoy *et al.*, 2018). In particular, Ti6Al4V is being intensively investigated for selective laser melting (SLM), which has the best feature resolution among metal additive manufacturing methods (Sames *et al.*, 2016).

Titanium matrix composites (TMCs) are attractive due to their high melting point/strength, good corrosion resistance, and better wear resistance than titanium alloys (Attar *et al.*, 2018; Kondoh, 2015). The TMCs can be manufactured by two routes, namely *in situ* processing involving synthesis of reinforcement particles by reaction during manufacturing, or *ex situ* processing involving the addition of stable particles at the beginning of the process (Dadbakhsh *et al.*, 2019).

Ex situ manufacture enables a wider range of particle chemistries to be integrated into the TMCs. However, ultrafine reinforcement particles are desired for the best performance of *ex situ* composites, which can be expensive, require more safety measures during processing, and be prone to agglomeration (Dadbakhsh *et al.*, 2019; Yu *et al.*, 2019). Particles within *in situ* TMC composites, on the other hand, are typically in better thermodynamic equilibrium with the matrix, and exhibit clean and potentially aligned/coherent interfaces with the matrix (Dadbakhsh *et al.*, 2019) which is more desirable for stronger matrix- reinforcement bonding (Kainer, 2006). Additionally, *in situ* grown particles have the potential to be smaller in size and better distributed within the matrix, which makes *in situ* reinforcement more favourable than *ex situ* particle reinforcements (Dadbakhsh *et al.*, 2019; Kondoh, 2015; Tjong and Ma, 2000).

The manufacture of *in situ* TMCs has been successfully carried out by a range of routes including vacuum arc remelting (Ma *et al.*, 2017; Rielli *et al.*, 2019), powder metallurgy (Huang *et al.*, 2011), vacuum hot-press sintering (Sun *et al.*, 2017), vacuum induction melting (Kim *et al.*, 2011) and spark plasma sintering (SPS) (Bai *et al.*, 2019; Wei *et al.*, 2017) methods. Additive manufacturing methods have also been adopted for *in situ* TMC manufacturing, including laser deposition (Hu *et al.*, 2018; Zhang *et al.*, 2019), wire arc (Bermingham *et al.*, 2018) and SLM (Attar, Bönisch, Calin, Zhang, Zhuravleva, *et al.*, 2014; Dadbakhsh *et al.*, 2020; Gu *et al.*, 2011a; Gu, Shen, *et al.*, 2009).

SLM's rapid heating and cooling cycle (DebRoy *et al.*, 2018) potentially could improve reinforcement particle distribution within the matrix. Using SLM, *in situ* growth of TiC (Dadbakhsh *et al.*, 2020; Gu *et al.*, 2011a; Gu, Shen, *et al.*, 2009; Gu, Wang, *et al.*, 2009; Vrancken *et al.*, 2019) and TiB (Attar, Bönisch, Calin, Zhang, Scudino, *et al.*, 2014; Attar, Bönisch, Calin, Zhang, Zhuravleva, *et al.*, 2014; He *et al.*, 2019; Kühnle and Partes, 2012; Patil *et al.*, 2019) have been investigated. *In situ* TiC synthesis has been used with Ti (Gu *et al.*, 2011a), Ti-Al (Gu, Shen, *et al.*, 2009; Gu, Wang, *et al.*, 2009) and Ti-Mo (Dadbakhsh *et al.*, 2020; Vrancken *et al.*, 2019) matrices. Depending on the TMC manufacturing method the feedstock material chemistry and morphology needs to be carefully optimised, usually by powder processing.

Direct mixing and ball milling are typical TMC powder feedstock preparation methods (Yu *et al.*, 2019). Ball milling produces a homogeneous particle intermixing; however, particle deformation causes flowability issues (Kühnle and Partes, 2012). On the other hand, direct mixing generates limited particle deformation due to reduced mechanical damage, but provides restricted particle intermixing (Yu *et al.*, 2019). Sufficient flowability is essential for the SLM process to provide uniform coverage of the whole layer (Gu *et al.*, 2012) and the morphology of the powder feedstock is crucial for powder flowability and packaging behaviours (Zhang and Attar, 2016). Therefore, an efficient powder preparation methodology providing spherical particles and homogeneous chemistry is an essential step of SLM processing.

In summary, there is an urgent need to develop a methodology for composite powder feedstock preparation that addresses challenges including powder flowability, morphology, cost-effectiveness, handling, and mixing. Furthermore, for the case of Ti6Al4V TMCs reinforced by TiC particles, detailed analysis of TiC formation, its effect on microstructure, and the dynamics of porosity formation and solidification in these composites is pivotal in understanding their manufacturing mechanism and assessing their potential for broader applications.

In this study, we investigate the manufacture of Ti6Al4V-TiC TMCs via SLM, using an *in situ* reaction of Ti with carbon. Ti6Al4V powders are pre-mixed with graphite flakes using a direct mixing method to retain spherical particle morphology and flowability (Bai *et al.*, 2019). Graphite flakes are used as carbon source, which is low-cost, may aid powder flow during mixing by acting as a lubricant. The pre-prepared composite Ti6Al4V-carbon powders are processed by SLM using a pulsed laser with a range of processing parameters within the field of 57–87J/mm^3 volumetric energy density. The microstructure and properties of the resulting Ti6Al4V-TiC TMCs are characterised, including evaluation of porosity and hardness, to determine the optimum SLM processing parameters.

2 Experimental Procedure

2.1 Powder Preparation

Pre-alloyed Ti6Al4V powder (grade 23, LPW Technology Ltd, UK, also referred to as 'Ti64') was used as the matrix material. The size distribution of the Ti6Al4V powder was measured by laser diffraction (Malvern Mastersizer 3000), and D10, D50 and D90 were measured as 21.7μm, 31.6μm and 45.3μm, respectively. The particle size range was within the recommended range for selective laser melting (SLM) (DebRoy *et al.*, 2018). Graphite flakes with 7-10μm flake diameter (99%, metals basis, Alfa Aesar, USA) were used as the carbon source. The Ti6Al4V powder was mixed with 1wt.% of graphite flakes using a planetary ball mill (PM100, RETSCH GmbH, Germany) for 60 minutes at a speed of 500rpm.

2.2 SLM processing

The pre-mixed Ti6Al4V+graphite powders were processed using a Renishaw AM125 selective laser melting system. A 30μm thick layer of powder was laid down onto a titanium substrate plate, and selected parts of this layer were melted in argon atmosphere according to the sliced geometry data using a pulsed laser source. The meander scanning strategy was used with 67° rotation of laser lines for each successive layer. SLM samples were manufactured with 2mm height and 15mm×15mm base area (Figure 1(b)). 15 samples were made, with a range of laser

pulse duration (exposure time), distance between laser pulses (point distance) and hatch spacing combinations to investigate processing optimisation. Box-Behnken response surface methodology and the Minitab software package were used for analysis. A separate plain Ti6Al4V alloy sample was additionally manufactured using optimised parameters. Table I summarises the parameters used for SLM processing of the 16 samples. The laser power was set to 200W for all samples. Processed samples were removed from the baseplate using wire erosion.

Volumetric (E_v) and linear (E_l) energy densities have been calculated using equations 1 and 2, respectively (Cherry *et al.*, 2014; Harrison *et al.*, 2015), where P is laser power, t_{exp} is exposure time, x_{pd} is point distance, h is hatch space, and l is layer thickness. The average travel speed v (equation 3) is used to convert the pulsed laser's movement to the continuous laser's speed (Freeman, 2018), where c is the laser's jump speed, fixed as 4.1m/s for the Renishaw AM125. Equation 4 is used to calculate pore sphericity (Ψ) from X-ray computed micro-tomography (microCT) data, with V_p pore volume and A_p pore area.

$$E_v = \frac{P \times t_{exp}}{x_{pd} \times h \times l} \tag{1}$$

$$E_l = \frac{P \times t_{exp}}{x_{pd}} \tag{2}$$

$$v = \frac{x_{pd}}{t_{exp} + (\frac{x_{pd}}{c})} \tag{3}$$

$$\Psi = \frac{\pi^{\frac{1}{3}} \times 6V_p^{\frac{2}{3}}}{A_p} \tag{4}$$

Table I. SLM processing parameters for (1-15) TiC reinforced Ti6Al4V samples, and (16) plain Ti6Al4V sample.

Sample Number	Hatch Space (µm)	Exposure Time (µs)	Point Distance (µm)	Volumetric Energy Density (J/mm³)	Linear Energy Density (J/mm)	Average Travel Speed (mm/s)
1	90	60	63.5	70	0.189	841
2	110	60	63.5	57.3	0.189	841
3	90	74	63.5	86.3	0.233	710
4	110	74	63.5	70.6	0.233	710
5	90	67	57	87.1	0.235	705
6	110	67	57	71.2	0.235	705
7	90	67	70	70.9	0.191	833
8	110	70	67	63.3	0.209	776
9	100	60	57	70.2	0.211	771

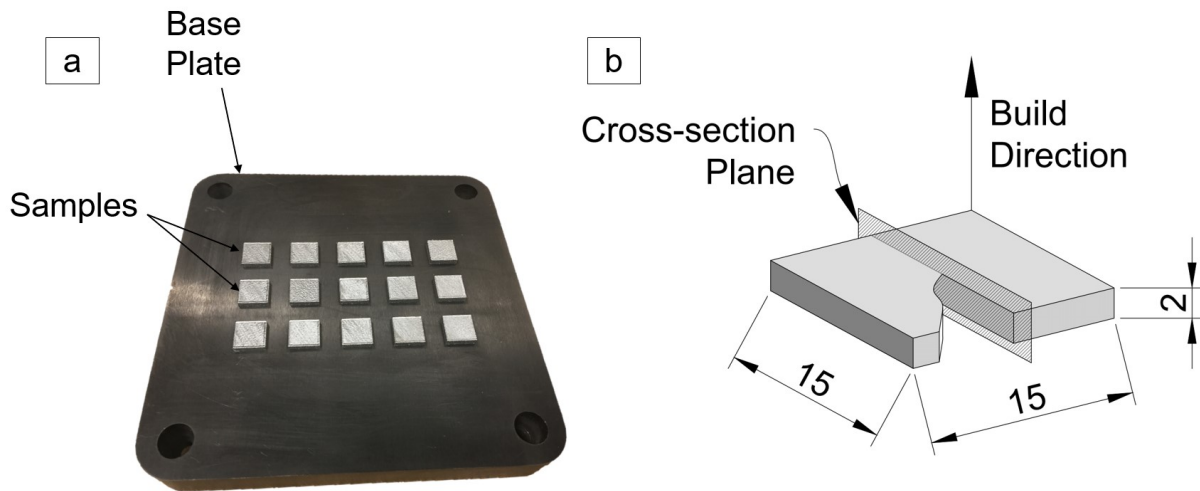|						
10	100	74	57	86.5	0.26	648
11	100	60	70	57.1	0.171	908
12	100	74	70	70.5	0.211	769
13	100	67	63.5	70.3	0.211	770
14	100	67	63.5	70.3	0.211	770
15	100	67	63.5	70.3	0.211	770
16: Plain Ti6Al4V	95	70	60	81.9	0.23	709

Figure 1. (a) processed parts on the SLM baseplate, (b) sample dimensions and the cross-sectional surface used for SEM, microhardness and optical porosity measurements.

2.3 Materials Characterisation

Powder morphology and the microstructure of SLM parts were examined using a field emission gun scanning electron microscope (Inspect F50 FEG-SEM, FEI, USA). Samples were cut through parallel to their build direction (Figure 1(b)), and these cross-sectional surfaces were used for optical imaging, SEM imaging, and microhardness measurements. Vickers microhardness was measured using a 500g load with a 10-second dwell time (Durascan, Struers, USA). An average of seven measurements was taken to determine the hardness for each sample. An X-ray diffractometer (XRD; D2 Phaser, Bruker, Germany) was used for phase analysis of powders and bulk samples, using Cu-Kα radiation at 30kV, step time of 0.2s, step size of 0.02°, and a 20°-90°(2θ) scanning window.

The relative porosity of Ti6Al4V-TiC composite materials was measured in 2D using optical cross-sectional imaging (Eclipse ME600, Nikon, Japan) and in 3D using X-ray computed tomography (μCT). Optical cross-sectional images were stitched together and 6200μm×600μm areas were examined for assessment of areal porosity parallel to the SLM build direction. Optical images were converted to a binary black (pore) and white (matrix) contrast images using Fiji/ImageJ software's FijiJ distribution (Schindelin *et al.*, 2012). The areal porosity ratio and pore morphology were assessed for each sample, with areas smaller than 5μm^2 not included to reduce noise. In addition, 3D volumetric porosities in cross-sectional samples were analysed

5

by μCT using a ZEISS Xradia 620 Versa X-ray Microscope (XRM) housed within the Sheffield Tomography Centre (STC) at The University of Sheffield, UK. The set up includes a CCD detector system with scintillator-coupled visible light objective lenses and a tungsten transmission target. Parameters used include an X-ray tube voltage of 110kV and a tube current of 141μA using the 4x objective lens, HE4 filter, 2401 projections resulting in a voxel (3D pixel) size of 0.85μm. Tomograms were reconstructed from 2D projections using ZEISS XMReconstructor software, and the reconstructed data was analysed and visualised using ORS Dragonfly software version 2020.2. Pores consisting of less than 50 voxels were removed to reduce noise.

To evaluate phase distribution, texture, and α–β phase relationships, electron backscattered diffraction (EBSD) analysis was performed with a FEG-SEM (JSM 7900F, JEOL, Japan) equipped with an EBSD detector (Aztec HKL Advanced Symmetry System, Oxford Instruments, UK) using 20.00kV accelerating voltage and 0.06μm step size. AZtecCrystal software (version 2.1, Oxford Instruments, UK) and MATLAB toolbox MTEX (Bachmann *et al.*, 2010) were used for data analysis and parent grain reconstruction (Niessen *et al.*, 2021).

3 Results

3.1 Feedstock Powder

SEM was used to examine morphologies of parent Ti6Al4V particles and graphite flakes (Figure 2). The gas atomised Ti6Al4V particles had mainly spherical morphology and were < 55 mm in size. Some irregularly shaped Ti6Al4V particles (Figure 2(a)) and small satellite particles (smaller than 10μm and spherical in shape) adhered to bigger ones were observed (Figure 2(a,c), white arrows), which are typical for the gas atomisation process (Ahsan *et al.*, 2011).

Direct mixing of the parent Ti6Al4V particles and graphite flakes in the planetary ball mill for 1 hour caused coating of parent Ti6Al4V particles by carbon (Figure 3), and led nearly continuous carbon coverage, however a graded SEM-SE contrast pattern was observed due to varying coating thickness of carbon over the parent Ti6Al4V particles (Figure 3(b)). Thicker carbon coated regions appear darker, emitting fewer secondary electrons (SE) than regions with thinner carbon coating where SE also originate from the underlying Ti6Al4V. Higher magnification imaging shows that the original graphite was highly deformed, and an adhered film consisting of agglomerated carbon nanoparticles was fabricated (Figure 3(d)). The joins between satellite-parent particles are shielded from mechanical compression during direct mixing, causing a reduced carbon coverage band around joint regions (Figure 3(a,c), white arrows).

After 1 hour mixing, independent residual carbon particles with disc-like morphology were observed (Figure 3(a), yellow arrows). This morphology was different from the original graphite flake particles (Figure 2(d)). During 1h mixing, repetitive compression and fracture impacts from larger and harder Ti6Al4V particles will result in morphology change and shrinkage of the original graphite flake particles.
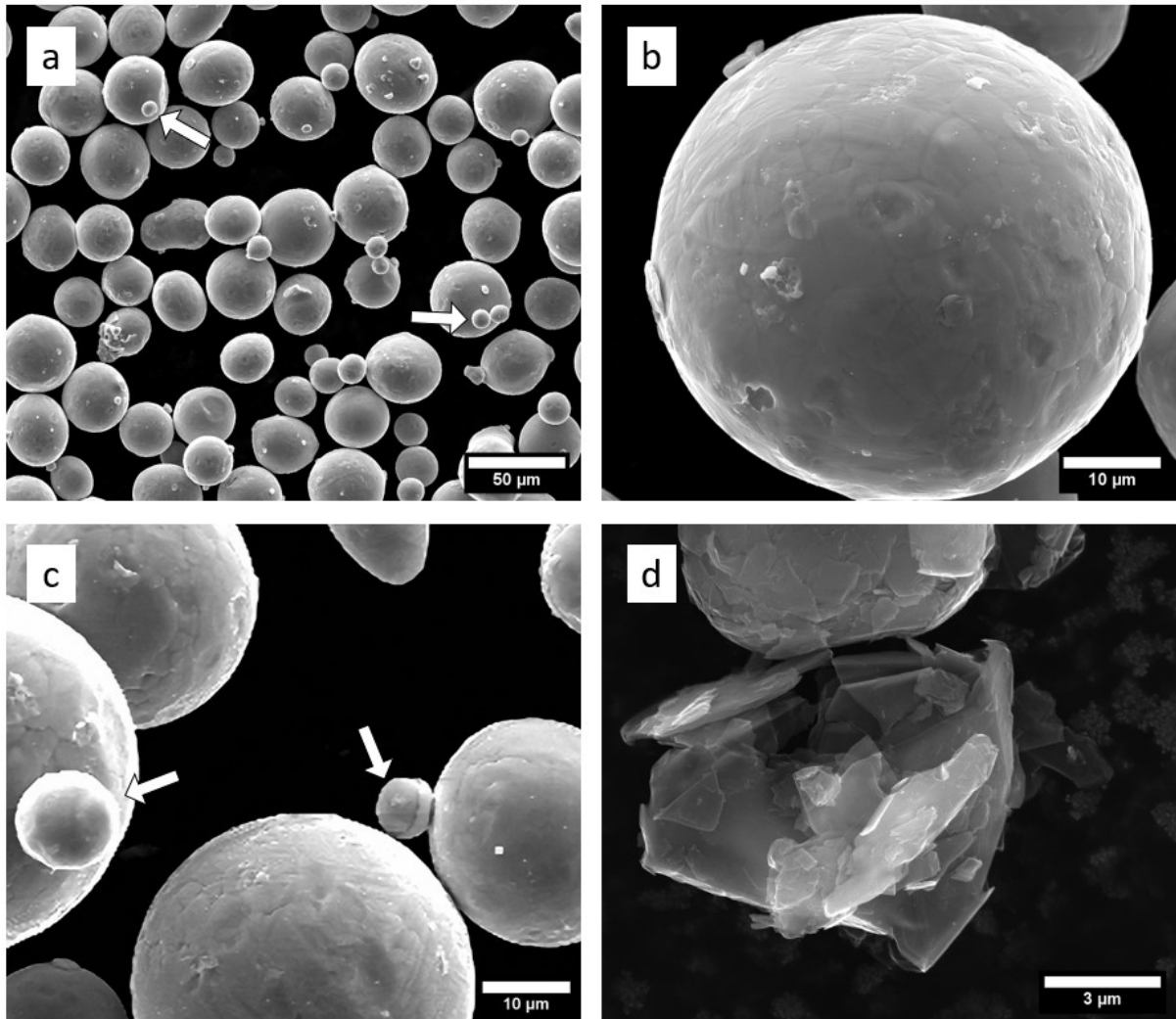
Figure 2. Secondary electron SEM images of (a,b) pre-alloyed Ti6Al4V particles, (c) satellite particles on parent Ti6Al4V particles, and (d) graphite flake particles. White arrows indicate examples of Ti6Al4V satellite particles.

X-ray diffraction (XRD) was utilized to examine the alteration of graphite particles during mixing. XRD patterns of graphite flakes, parent Ti6Al4V powder and mixed Ti6Al4V-carbon composite powder are given in Figure 4. No signs of chemical reaction, such as crystalline TiC formation, was observed for the composite powder. The graphite (0002) peak disappeared after 1h mixing, consistent with transformation of graphite flakes to amorphous carbon nanoparticles.

Ti6Al4V particles retain good crystallinity after 1h of mixing (Figure 4), which is expected due to their hardness relative to the softer graphite flake particles in the mixture. Additionally, the Ti6Al4V particles preserved their spherical shapes after 1h mixing, which is significant for the flowability of the Ti6Al4V-carbon powder to be used as SLM feedstock.
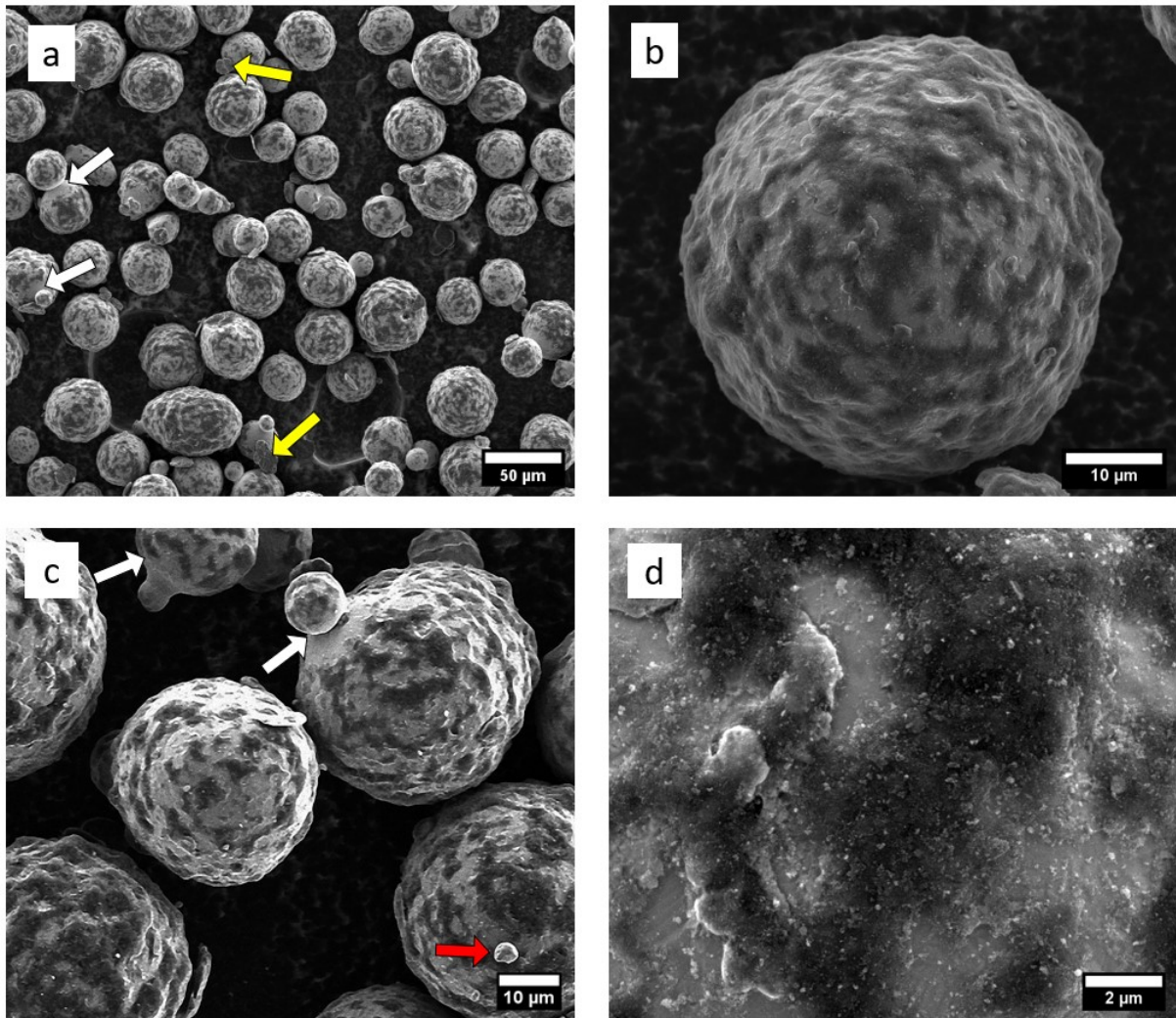
Figure 3. Secondary electron SEM images of mixed Ti6Al4V-carbon composite powder feedstock: (a) Parent Ti6Al4V particles coated by carbon. Residual graphite flake discs after mixing are dispersed in the powder (e.g. yellow arrow). Satellite particles (white arrows) are still attached to larger Ti6Al4V particles; (b) carbon coated Ti6Al4V particle with graded dark-grey/light-grey contrast due to varying carbon coating thickness; (c) Uncoated/carbon deficient zones around particle junctions (white arrows); (d) Surface of carbon coated Ti6Al4V particle with adhered carbon nanoparticle agglomerates.
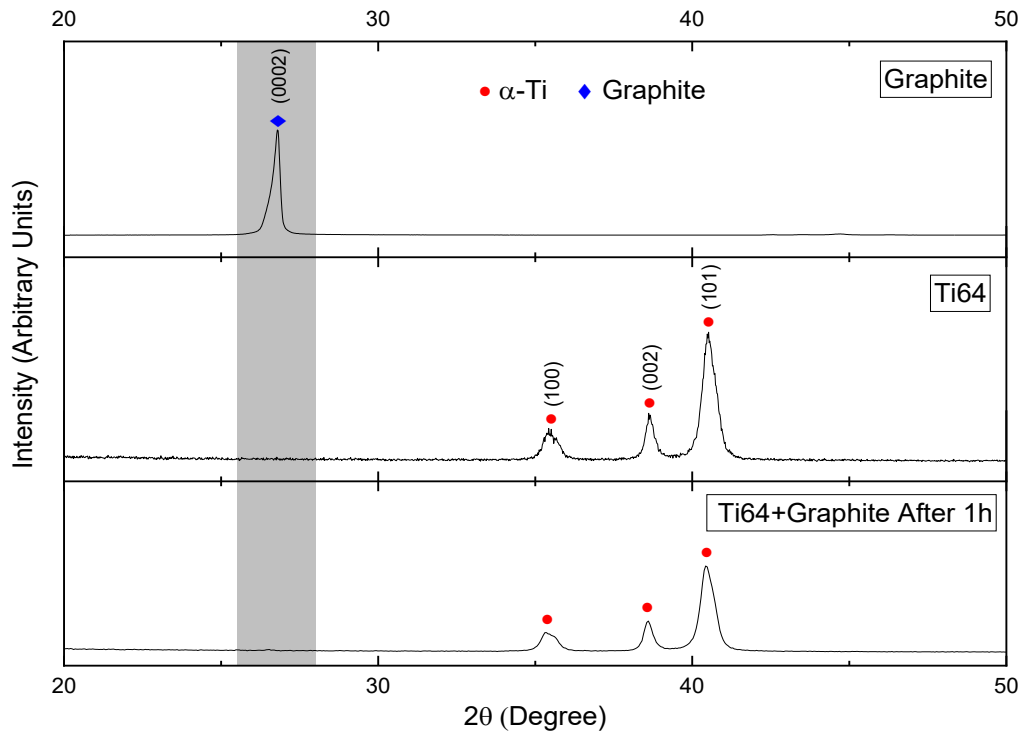
Figure 4. XRD patterns of Graphite flakes, parent Ti6Al4V powders (Ti64), and 1h mixed Ti64+graphite.

3.2 SLM Processed Ti6Al4V Composites

3.2.1   Porosity of SLM Ti6Al4V Composites

The relative porosity of the SLMed Ti6Al4V-carbon composites measured from optical cross-sectional images varied between 3.6%-0.5%, corresponding to a relative density range of 96.4%-99.5%. p-values (Montgomery, 2017) of hatch distance, exposure time and point distance were 0.022, 0.046 and 0.035, respectively, indicating that hatch distance, exposure time and point distance are all effective variables on porosity. Porosity change with varying volumetric energy density is given in Figure 5(e). Increasing the energy density led to higher relative density; however, the highest relative density was observed at medium energy densities of 70.2J/mm^3 and 70.3J/mm^3. There was a higher than expected porosity for 70.6J/mm^3 energy density sample.

Lowest energy densities generated significantly higher porosities. Types of pore morphologies observed in the Ti6Al4V-carbon composites are illustrated in Figure 5 and Figure S1. Large irregular pores in the low energy density samples can be seen in Figure 5(a,b), and low energy density samples have more pores for all pore size ranges (Figure S2). Partially molten particles can be identified in low and medium energy density samples (Figure 5(a,b,c)). Increasing the energy density resulted in less irregularly shaped pores; however, occasional particle edges can still be observed (dashed square in Figure 5(d)). Planar defects randomly distributed within the structure (Figure 5(c,d)) arise from unreacted/undissolved carbon residues (Section 3.2.2).

X-ray CT (μCT) has been used to investigate distribution of pores in 3D for low (57.3J/mm^3) and medium (70.3J/mm^3) energy density Ti6Al4V-carbon composite samples. Volumetric relative porosities are calculated as 5.0% and 1.1% for 50.7J/mm^3 and 70.3J/mm^3, respectively, which is a 78% porosity reduction with 57.3J/mm$^3 \rightarrow$ 70.3J/mm^3. The 3D pore distributions,

reconstructed from μCT images with a 0.85μm³ voxel size, are shown in Figure 6(a,b) with pores > 50 voxels plotted. Consistent with the 2D analysis, pore size and count decreased with increased energy density.

The frequency of pores within different pore volume ranges for low (57.3J/mm³) and medium (70.3J/mm³) energy density samples is shown in Figure 6(e). An incremental binning size is used to illustrate the information clearly because the quantity of pores reduced significantly with increasing size. 10μm³, 100μm³, 1000μm³ and 10,000μm³ binning size range was chosen for 30-100μm³, 100-1000μm³, 1000-10,000μm³ and 10,000-100,000μm³ pore volume ranges, respectively. The total number of pores was measured as 1350 for 53.7J/mm³ energy density and as 391 for 70.3J/mm³ energy density, for the same XCT analysis volume of 1.7×10^8 μm³. The total pore number reduced by 71% with 57.3J/mm³ → 70.3J/mm³, and a reduction observed for all pore size categories (Figure 6(e)).

The 3D μCT porosity analysis revealed that irregularly shaped convoluted pores with a larger size than the original powder particles are present in the low energy density sample (57.3J/mm³). These arise due to insufficient energy of the laser to melt the whole powder layer. An example of a large pore with ~200μm diameter (volume of ~960,000μm³) is illustrated in Figure 6(c). Such pores are aligned parallel to the SLM building direction because they exist over more than one layer (Figure 6(a)).

In comparison, the medium (70.3J/mm³) energy density Ti6Al4V-carbon composite sample has smaller pores than original particle size (Figure 6(b)). Additionally, pores become more spherical with increasing energy density (Figure 6(d)). However, a subset of pores still have inner concave surfaces (Figure 6(b), Figure 5(d)). This type of pore are associated with insufficient local laser energy density (Kasperovich *et al.*, 2016) and the concave surfaces likely originate from insufficiently molten particles.
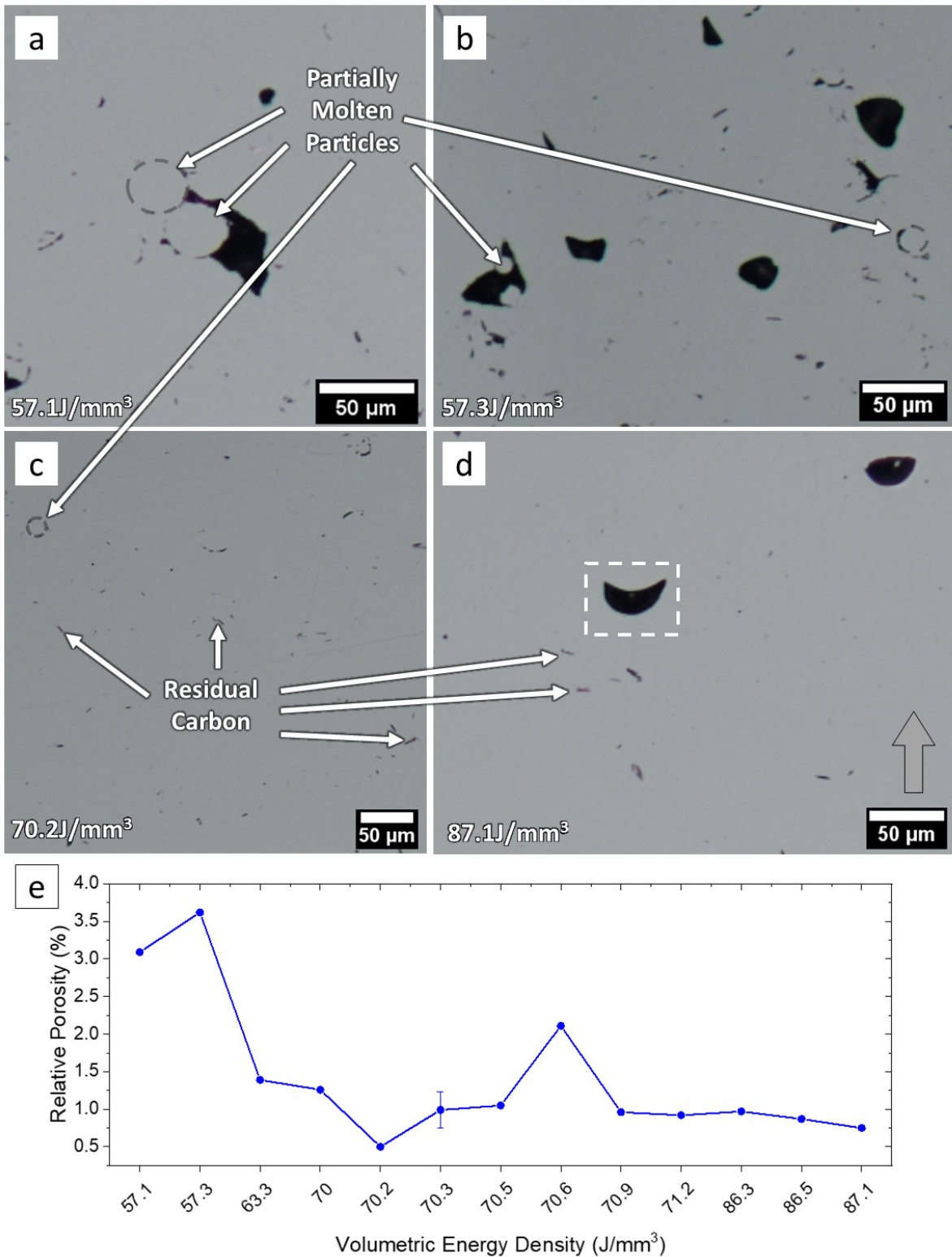
Figure 5. Representative optical images showing porosity defects in Ti6Al4V-carbon samples with different volumetric energy density levels: (a) 57.1J/mm³, (b) 57.3J/mm³, (c) 70.2J/mm³, (d) 87.1J/mm³. Typical defect types (partially molten particles, residual carbons, lack of fusion pores) are highlighted. Lower right arrow shows SLM build direction for all images. (e) Relative porosity of Ti6Al4V-carbon parts obtained from 2D optical image analysis at different volumetric energy densities (error bar represents standard error for multiple samples at the same energy density).

Figure 6. 3D pore distribution of a (a) low energy density (57.3J/mm³) and a (b) medium energy density (70.3J/mm³) Ti6Al4V-carbon samples measured 3D imaging by μCT. (c) Detailed view of the largest pore (red) in (a) highlig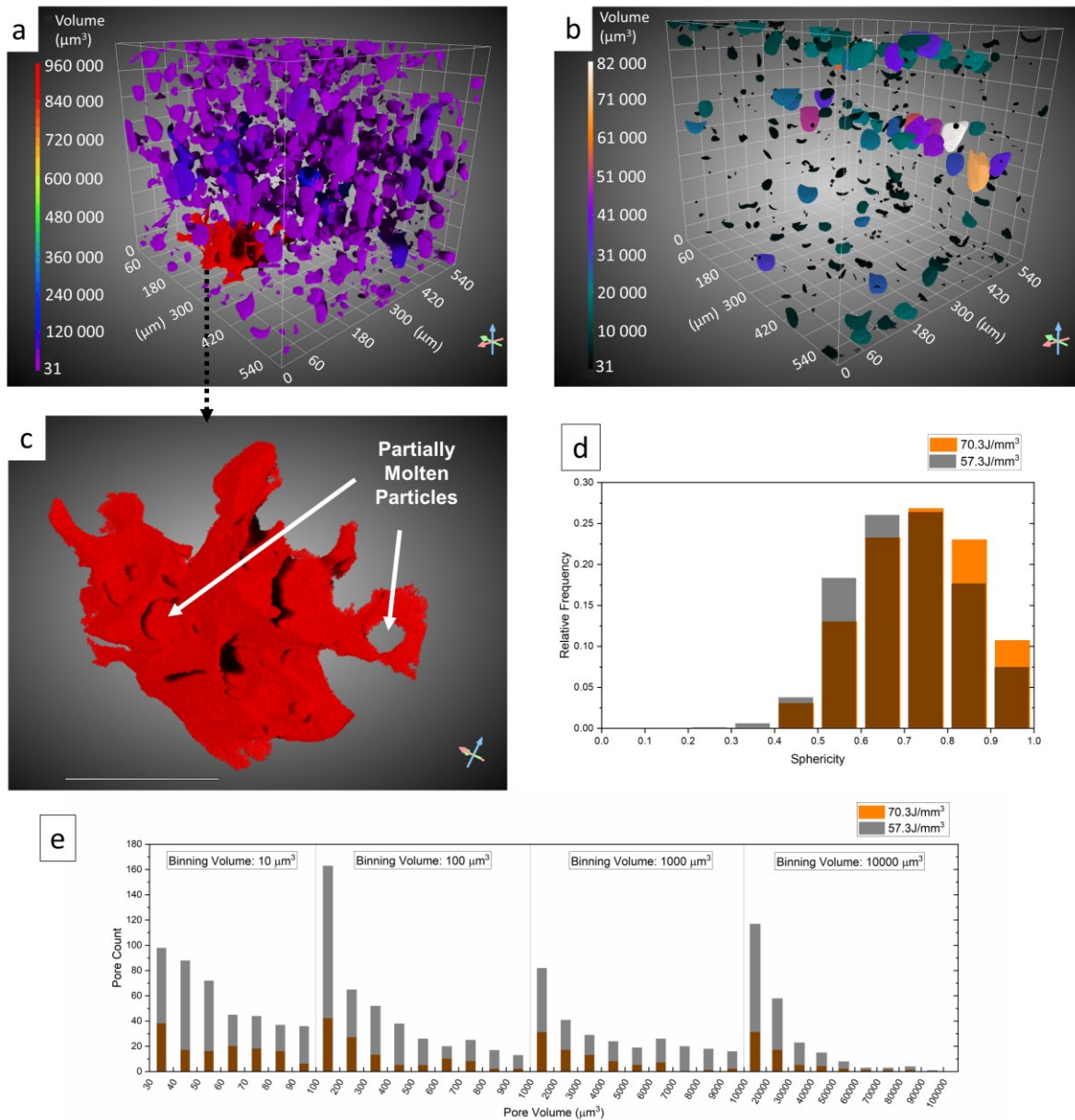hting partially molten particle defects (scalebar represents 100μm). (d) Change of pore sphericity for (a,b), and (e) frequency of pores in different size ranges from (a,b). The light blue arrow in (a,b,c) indicates the SLM build direction.

3.2.2 Composite Microstructure

XRD and SEM were used to identify the phases present within the *in situ* Ti6Al4V-carbon composites. XRD patterns of a Ti6Al4V-carbon composite (70.3J/mm³), plain Ti6Al4V sample without any carbon addition and parent Ti6Al4V powder are given in Figure 7. The Ti6Al4V powder, plain SLM Ti6Al4V and Ti6Al4V-carbon composite have an α/α′-titanium structure, and no β-titanium peaks were detected by XRD. TiC peaks were identified in all composite samples confirming the *in situ* Ti-C reaction and formation of crystalline TiC (cubic Fm-3m). TiC is a non-stoichiometric compound and can be formed within a C/Ti composition range between 0.5 and 1 (Storms, 1967). Hence, for 1wt.% carbon added here, TiC could potentially form up to 9.9wt.% TiC in the matrix. Hereafter the SLM composite is described as a Ti6Al4V-TiC composite.

The Ti6Al4V-TiC composites' microstructure was examined using SEM and EDS. A fine sub-micron dispersion of TiC particles with sizes ~0.1-1µm was identified within the Ti6Al4V matrix (Figure 8(b,c)), with some local concentration of TiC in dense particle clusters (Figure 10(a)). The high carbon concentration within the TiC particles measured by SEM-EDS chemical mapping is consistent with the TiC formation identified by XRD (Figure 4). In addition, occasional residual flakes of carbon were observed, coated in a continuous layer of nucleated TiC particles ((Figure 8(d)). The volume of residual carbon/TiC regions was estimated for the SLM composite region in Figure 5(c) (medium 70.2J/mm^3 SLM energy density, with low porosity) using the same method for relative porosity estimation. The residual graphite flake (with TiC coating) volume was measured as ~0.3vol.% from this image, which is equivalent to ~0.14wt.%, and with the actual residual graphite volume lower than this. The mechanisms of growth of TiC in these different morphologies are discussed in Section 4.2.2.
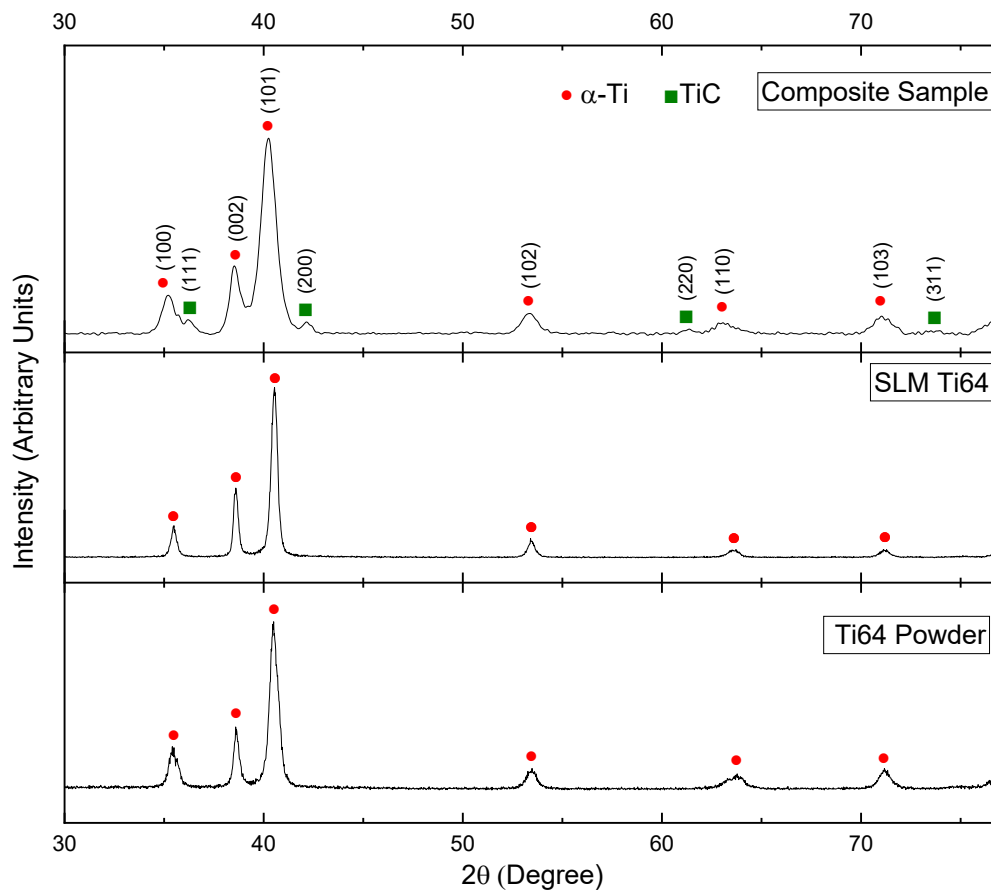

Figure 7. XRD patterns of SLM processed Ti6Al4V-TiC (Composite Sample, 70.5J/mm^3 energy density), plain Ti6Al4V alloy (SLM Ti64) and parent Ti6Al4V powder. The phases identified are α-Ti (red spots) and TiC (green squares).
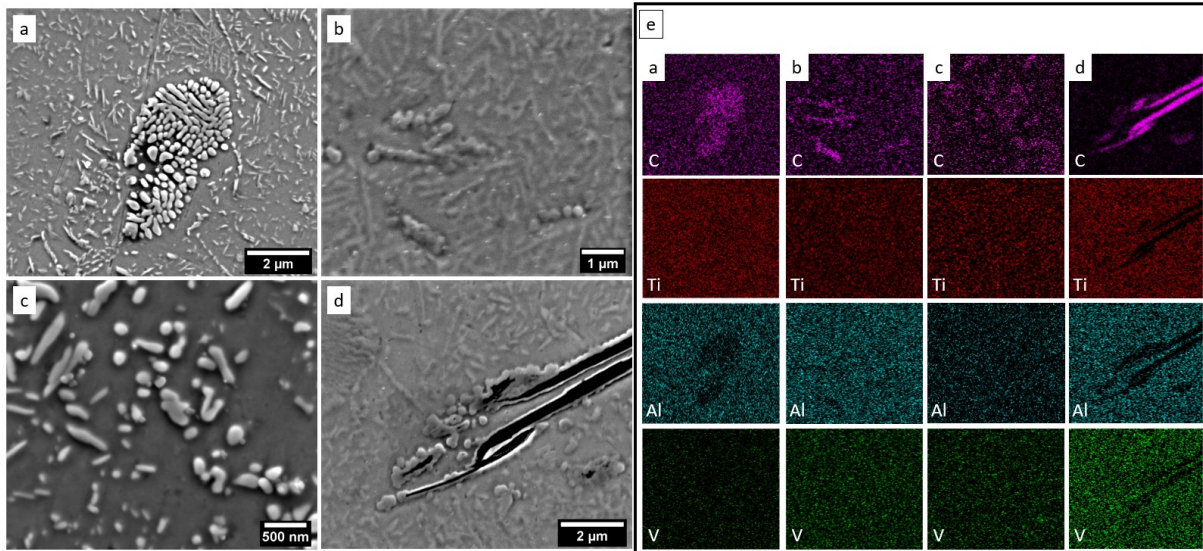
Figure 8. (a-d) Secondary electron SEM images showing TiC particles dispersed within the Ti6Al4V matrix in a Ti6Al4V-TiC composite processed using 70.3J/mm³ volumetric energy density. (e) EDX maps of C, Ti, Al and V for images (a-d).

EBSD analysis was used to examine the structure of the α-Ti6Al4V matrix in more detail. The inverse pole figure (IPF) from the EBSD analysis performed on medium energy density sample (70.3J/mm³) is given in Figure 9(a). The SLMed Ti6Al4V has a martensitic microstructure (α′) due to the rapid cooling rate of the SLM process, consistent with previous work (Simonelli *et al.*, 2014a). Reconstruction of the prior parent β grains from Figure 9(a) according to the orientation relationship ($(0001)_\alpha$ // $(110)_\beta$ and $\langle 11\overline{2}0 \rangle_\alpha$ // $\langle 111 \rangle_\beta$) is given in Figure 9(b). Columnar β grains, due to high heat transfer through the solid base plate, was observed. This type of solidification microstructure has been reported (Simonelli *et al.*, 2014a, 2014b); however here the β column width of ~5μm in the area analysed is significantly smaller than previous reports. An average column width of 103±32μm was reported by Simonelli et al. (Simonelli *et al.*, 2014a).

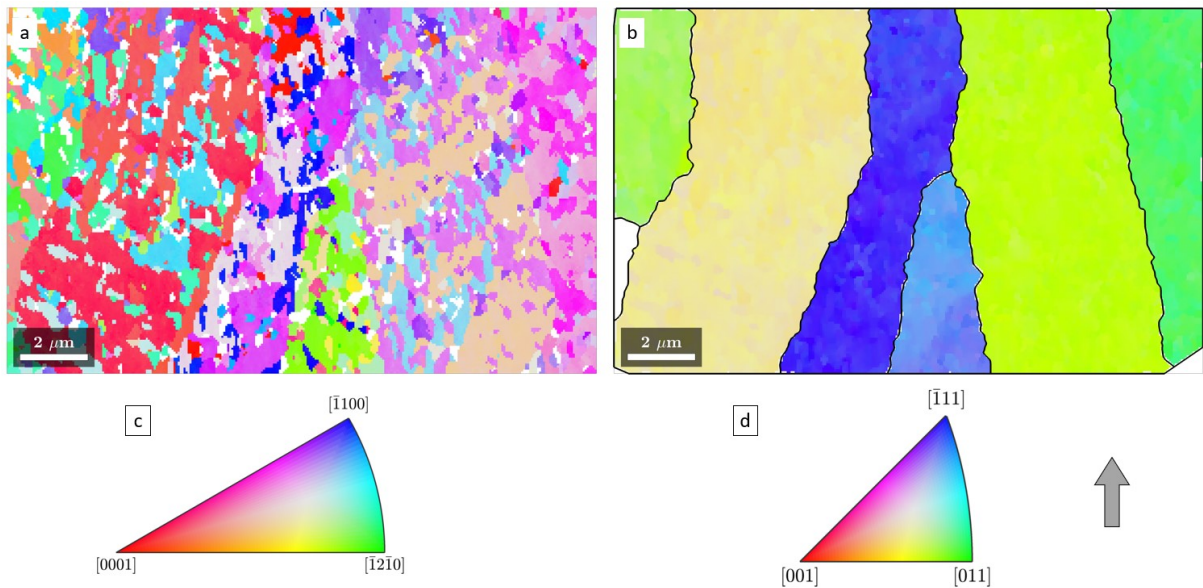*Figure 9. EBSD inverse pole figure (IPF) map of α'-Ti6Al4V matrix of SLM Ti6Al4V-TiC composite processed using 70.3J/mm³ volumetric energy density; (b) reconstructed parent β grains from (a) according to the α–β orientation relationship; IPF colour keys for orientations of (c) α'-HCP phase and (d) β-cubic phase. The lower right arrow indicates the SLM build direction.*

14

3.2.3 Hardness

Hardness of the SLM Ti6Al4V-TiC composites was measured parallel to the build direction (Figure 1(b)) using 500 g load. The Ti6Al4V-TiC composites' hardness was within the range 422 HV - 459 HV, compared to 420 HV of a plain SLM Ti6Al4V sample processed using the same equipment and parent alloy powder (Figure 10, Figure S3).

Response surface regression revealed that p-values (Montgomery, 2017) for hatch distance, exposure time and point distance are 0.298, 0.016, and 0.030, respectively when the confidence level was set at 95%. This indicates that SLM exposure time and point distance affected Ti6Al4V-TiC composites' hardness, whereas no relationship was present between hatch distance and hardness for the chosen parameter range.

SLM exposure time and point distance define an average laser travel speed (Equation 3), and hardness change of Ti6Al4V-TiC composites as a function of average laser travel speed is shown in Figure 10. Increasing the average laser travel speed (shorter exposure time and longer point distance) reduces the laser energy input per volume. When the average laser travel speed was high (908 mm/s), the hardness of unreinforced Ti6Al4V and the Ti6Al4V-TiC composite was similar (422 HV vs 420 HV). On the other hand, decreasing the average laser travel speed and thereby increasing the laser energy input increases the Ti6Al4V-TiC composite hardness indicating improved mechanical properties. No relationship between relative porosity and hardness was observed because pores were avoided during hardness measurements.
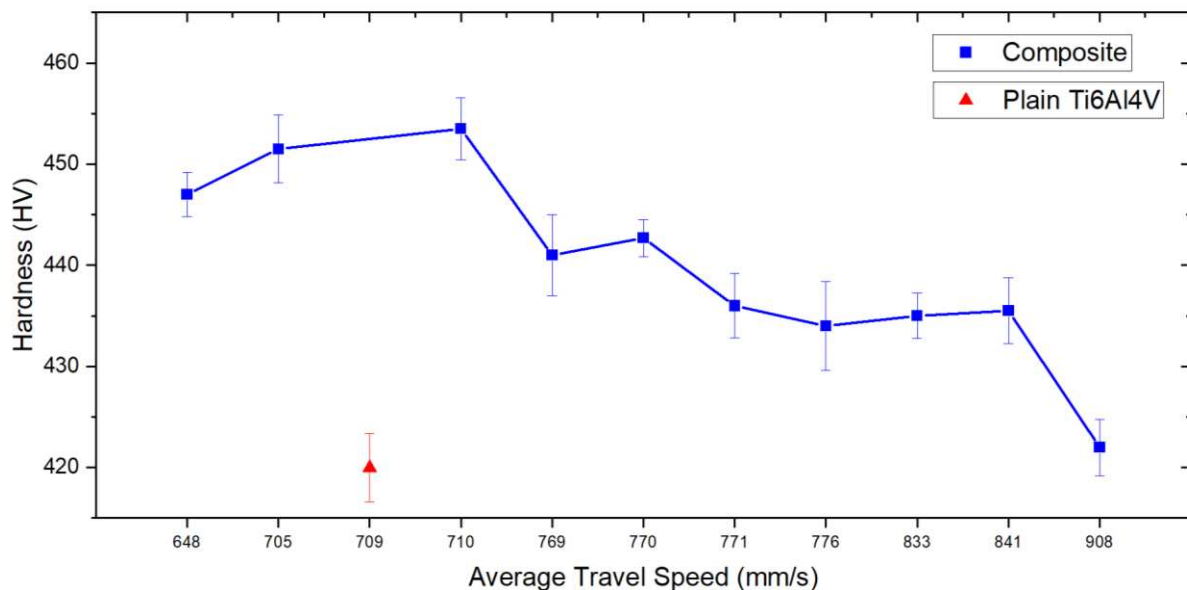
Figure 10. Change of Ti6Al4V-TiC hardness for varying average laser travel speed (error bars represent standard error).

4 Discussion

4.1 Powder Mixing

The additive manufacture SLM process involves laying down powder layer by layer, therefore powder flowability is a key parameter to enable the production of a homogeneously coated layer prior to laser melting (Gu *et al.*, 2012). Deformation of particles may cause powder flowability reduction (Kühnle and Partes, 2012), as well as modifying optical and thermal

properties of particles due to damage arising from impacts of milling balls (Yu *et al.*, 2019). The direct powder mixing method used in this study generated spherical Ti6Al4V powder feedstock with a near-continuous nanoparticle carbon coating. One of the biggest drawbacks of direct mixing is insufficient chemical mixing of input powders prior to processing (Gu *et al.*, 2014; Yu *et al.*, 2019). Here, the use of direct mixing with graphite flake feedstock particles was beneficial, redistributing the carbon whilst retaining the spherical Ti6Al4V particle shape, but still with sufficient particle impact energy to break the graphite up into amorphous carbon nanoparticles. Furthermore, the coating structure of nanosized carbon particles may help the subsequent rapid dissolution of carbon into liquid titanium matrix, providing a chemically homogeneous liquid before the solidification.

Ball milling is predominantly used for powder mixture preparation of ex situ composites (Yu *et al.*, 2019). For TiC-Ti6Al4V, the effect of initial TiC reinforcement particle size on mechanical properties and reinforcement distribution within the Ti6Al4V matrix has been studied by Wang et al. (Wang *et al.*, 2018). Smaller reinforcement particle sizes were reported as better for mechanical properties and achieving more homogeneous reinforcement distribution, and further studies investigated using nanosized TiC as ex situ reinforcement in CP-Ti and Ti6Al4V matrixes (Gu *et al.*, 2011b; Kun *et al.*, 2017). However, composite fabrication using nanosized TiC powders brings certain difficulties; the cost of the raw material increases, and handling and storage of these particles becomes more difficult due to their high reactivity and tendency to be suspended in the air. Here, nanosized TiC is formed *in situ*, removing these handling difficulties. In addition, the *in situ* synthesis of TiC nanoparticles generates cleaner reinforcement-matrix interfaces with stronger bonding, thermodynamically more stable particles, and a more uniform reinforcement particle distribution (Dadbakhsh *et al.*, 2019).

4.2 SLM Processing

4.2.1 Relative Porosity Change

The relative porosity of the Ti6Al4V-TiC composites varied between 0.5%-3.6% (Figure 5(e)) determined by 2D optical image analysis. The lower energy density samples (57.1J/mm^3 and 57.3J/mm^3 energy densities) showed high relative porosity, with large and irregular pores accompanied by partially molten particles (Figure 5(a,b), Figure 6(a)). This type of defect (Figure 6(c)) are called lack of fusion (LOF) defects and are mostly associated with insufficient laser energy which cannot melt whole powder layer (Gong *et al.*, 2014; Kasperovich *et al.*, 2016; Vilaro *et al.*, 2011). LOF defects are identified as the most destructive defect type on mechanical properties (Günther *et al.*, 2017; Kasperovich *et al.*, 2016); therefore, these should be avoided if possible.

Increasing the SLM energy density led to less frequent and smaller pores (Figure 5, Figure 6, Figure S1 and Figure S2). Additionally, the sphericity of pores increased, and the large irregular LOF defects disappeared (Figure 6(a,c,d)). However, spherical keyhole pores, associated with excessive energy density (Gong *et al.*, 2014; Kasperovich *et al.*, 2016), were not observed in any of the samples prepared here with different energy density levels. This was expected because the highest energy density used in this study (87.1J/mm^3) is not high enough to create spherical keyhole pores despite being within the range needed for nearly fully dense Ti6Al4V parts (Kasperovich *et al.*, 2016). However, pores with concave inner surfaces still were

observed even at the highest energy density (Figure 5(d)). These probably arose due to some degree of partial melting and LOF.

Presence of ceramic particles increases the viscosity of meltpool (Ma *et al.*, 2016; Yu *et al.*, 2019). Increased viscosity has been proposed as the reason for the need for higher energy density during the SLM manufacture of ex situ TMC composites (Attar, Bönisch, Calin, Zhang, Scudino, *et al.*, 2014; Gu *et al.*, 2011b). In this study, *in situ* growth of TiC particles within the meltpool took place. The meltpool's viscosity will be modified due to dissolved carbon, and will increase with the formation of TiC particles. The increase of viscosity triggers the balling effect and reduces the wetting of the previous layer (Gu *et al.*, 2011b; Shipley *et al.*, 2018). Increased energy input is then needed to provide sufficient wetting of the previous layer (Gu *et al.*, 2011b).

The minimum relative porosity of Ti6Al4V-TiC composites in this study, measured using optical analysis, was 0.5% at the highest energy density investigated ($87.1 J/mm^3$). This 99.5% relative density is higher than the relative densities of 98.2% (Kun *et al.*, 2017), 97% (Gu *et al.*, 2011b) and 98.5% (Gu *et al.*, 2014) which have been previously reported for ex situ TiC reinforced TMCs via SLM. These studies used 5wt.% (Kun *et al.*, 2017) and 15wt.% (Gu *et al.*, 2011b, 2014) TiC additions as the reinforcement. For the addition of 1wt.% carbon to Ti6Al4V used here, formation of TiC is expected within the range of 4.9wt.%-9.9wt.% depending on the Ti/C ratio (TiC stoichiometry) and assuming all carbon is consumed during *in situ* reaction. The 99.5% relative density of the Ti6Al4V-TiC composites fabricated here using *in situ* TiC formation is promising compared with the ex situ TiC reinforced composites.

4.2.2 Microstructure and Hardness

All SLM fabricated Ti6Al4V and Ti6Al4V-TiC composites had martensitic α′-titanium microstructures, with no β-titanium peaks detected by XRD (Figure 7). For the 1wt.% carbon addition used here, if all the carbon was consumed by Ti-C reaction to generate titanium carbide with the highest titanium content, i.e. $TiC_{0.5}$ (Storms, 1967), then the titanium proportion within the Ti6Al4V matrix would drop from 90wt.% to 89.1wt.% whilst the Al and V would increase to 6.5wt.% and 4.3wt.%, respectively. These Ti, Al and V proportions are still within the standard composition range of Ti6Al4V alloys (ASTM International, 2010). Additionally, in practise, some carbon (~0.14wt.%) remained undissolved as indicated by residual carbon patches in the processed material (Figure 5(c,d), Figure 8(d)) so the relative Ti, Al and V proportions will undergo less change. Hence, considering the influence of the *in situ* C-Ti reaction on the Ti6Al4V matrix microstructure, no change is expected from the original α′ microstructure of the SLMed Ti6Al4V matrix.

Sub-micron TiC particles with sizes ~0.1-1μm were distributed throughout the α′-Ti6Al4V matrix. The predominant TiC morphology was equiaxed TiC particles or short platelets (Figure 8). Occasional residual carbon platelets were observed coated in adjacent TiC particles (Figure 8(d)). Two different TiC formation mechanisms have been proposed depending on the meltpool temperature (Dadbakhsh *et al.*, 2020; Dunmead *et al.*, 1989). Dissolution of carbon within the liquid titanium and precipitation of TiC particles from the liquid has been proposed by Gu et al. (Gu *et al.*, 2014; Gu, Shen, *et al.*, 2009). On the other hand Dadbakhsh et al. (Dadbakhsh *et al.*, 2020), proposed that when the temperature remains below 2438˚C TiC directly formed through carburisation rather than first dissolving within the liquid.

The meltpool of the SLM process does not have a homogeneous temperature distribution (Hooper, 2018; Manvatkar et al., 2015); therefore, different temperature zones will be present within it. During the SLM processing here, some regions of the meltpool will have remained below 2438°C, while others will have surpassed this temperature. Consequently, both direct TiC formation and dissolution-precipitation mechanisms will have occurred. In the dissolution-precipitation mechanism, TiC nuclei precipitate from the liquid phase and TiC particles grow from these nuclei (Kun et al., 2017). The rapid cooling inherent to the SLM (Hooper, 2018) restricts grain growth, leading to the formation of sub-micron sized TiC particles. Here the fine TiC particles (<500μm) dispersed within the matrix (Figure 8(c)) are consistent with a dissolution-precipitation mechanism.

In contrast, the larger TiC particles and clusters observed in the SLM composites (Figure 8(d)) are consistent with direct carburization within the melt pool's cooler zones. In regions where temperatures remain below 2438°C, and with brief liquid Ti phase durations, the carbon clusters will not dissolve but instead directly react with titanium. This leads to the formation of larger TiC clusters or TiC particles surrounding a remaining carbon core, as seen in Figure 8(d,e).

In these SLM composites both in situ TiC formation mechanisms led to continuous Ti6Al4V-TiC interfaces without any evidence of interfacial voids, cracks or additional phases. The growth of TiC particles in situ thus ensures both very good matrix-particle bonding, and prevents contamination at the matrix-reinforcement interface which can occur with ex situ particle additions (Dadbakhsh et al., 2019). In addition, the submicron size of the in situ grown TiC particles will minimise any differential thermal strain arising during cooling, whilst maximising the potential for matrix hardening.

According to Ti-C phase diagram (Okamoto, 2006), solubility of carbon in liquid titanium drops significantly with reducing temperature. This may create a carbon-rich liquid next to solidification front. Therefore, the very last solidified regions would be rich in carbon. Localised dendritic TiC formation, as observed in Figure 8(a), may occur during dissolution-precipitation in regions solidified last with a high local carbon content.

Marangoni convection, arising from high temperature gradient and surface tension within the SLM meltpool, is an important aspect of SLM processing (DebRoy et al., 2018; Khairallah et al., 2016; Qiu et al., 2015), acting to homogenise chemistry and redistribute particles. Increasing Marangoni convection contributes to the homogeneous distribution of reinforcement particles within the matrix (Gu et al., 2011b, 2014; Hu et al., 2018), and it increases with increasing energy input (Hu et al., 2018; Yuan et al., 2015). In regions of low Marangoni convection, for example near the end of solidification at grain boundaries, TiC clusters will not be dispersed away from their growth location (Figure 8(a-c)).

Considering the α'-Ti6Al4V matrix, parent β grains elongated with the build orientation were identified from the reconstructed EBSD analysis (Figure 9(d)). This type of columnar parent β grain, extending through several SLM layers, is typical for Ti6Al4V alloys fabricated by SLM (Simonelli et al., 2014a). For the sample analysed, the widths (perpendicular to the build direction) of reconstructed columnar β grains were <5μm, which is significantly smaller than previously reported SLMed Ti6Al4V parent β grains with widths of size 103±32μm (Simonelli et al., 2014a). Smaller parent β grains are formed due to constrained grain growth caused by TiC particles (Yu et al., 2019). A similar tendency of grain refinement has been reported for AM of ex situ TiC reinforced Ti6Al4V by direct energy deposition (Liu and Shin, 2017).

The hardness of all the *in situ* Ti6Al4V-TiC composites was improved over the plain SLM Ti6Al4V alloy. The Ti6Al4V-TiC composites' hardness varied between 422HV and 459HV, compared to 420HV for plain Ti6Al4V in this study, and 391HV (Ali *et al.*, 2017) and 386HV (Ali *et al.*, 2018) in previous studies using the same parent Ti6Al4V alloy and SLM equipment. The presence of TiC particles can improve the strength of composite parts through the mechanisms of grain refinement, Orowan strengthening and increased dislocation density (AlMangour *et al.*, 2017, 2018; Ferguson *et al.*, 2014; Pan *et al.*, 2018; Wei *et al.*, 2017; Yu *et al.*, 2019). It is also likely that some residual solid solution carbon dissolved within the parent β-matrix, which is then incorporated into the α′-matrix by the diffusionless martensitic transformation. This solid solution carbon may further improve the hardness of the composite by solid solution strengthening.

The hardness of the Ti6Al4V-TiC composites varied with SLM processing parameters. Increasing SLM exposure time and decreasing point distance, which result in higher linear energy density and decreased average travel speed, generates composite microstructures with higher hardness (Figure 10). Further optimisation of the composite feedstock powder and SLM processing conditions, for example reducing the 1wt.% carbon content and/or using energy densities above 87J/mm^3 may lead to nearly fully dense Ti6Al4V-TiC composites with an optimised TiC content (eliminating residual carbon defects).

5 Conclusions

In this study, *in situ* TiC reinforced Ti6Al4V matrix composites have been fabricated using selective laser melting (SLM) of novel composite Ti6Al4V-carbon powders. The powder preparation method resulted in Ti6Al4V-carbon composite powder feedstock with minimal residue graphite flakes and a near-continuous amorphous carbon nanoparticle coating. The retention of spherical shape of the feedstock particles ensures that the composite Ti6Al4V-carbon powders are suitable for SLM processing.

The chosen SLM parameters, which resulted in energy densities between 57.1J/mm^3 and 87.1J/mm^3, significantly influenced the SLM Ti6Al4V-TiC composite relative density, porosity, and TiC formation. In particular, higher SLM energy density reduced porosity, rendering pores more spherical, minimizing large irregularities and reducing partially molten particles.

The resultant SLM Ti6Al4V-TiC composites demonstrated an increase in hardness (422-459HV) compared to the base Ti6Al4V processed by SLM. This enhanced hardness was largely due to the in situ growth of TiC nanoparticles, (predominantly ~0.1-1µm in size), whose fine dispersion throughout the Ti6Al4V α′-martensite matrix is effective in dispersion strengthening. Additionally, the TiC presence during solidification generates α′-Ti6Al4V grain refinement which will also contribute to the improved hardness of the Ti6Al4V-TiC composite.

In conclusion, this work has demonstrated the potential of a novel composite feedstock powder optimized SLM processing parameters for the manufacture of Ti6Al4V-TiC composites with low porosity, improved hardness and a nano-TiC dispersion strengthened microstructure. The composite feedstock preparation method is readily adaptable for different matrix and reinforcement materials in future studies.

6 Acknowledgement

7 References

Ahsan, M.N., Pinkerton, A.J., Moat, R.J. and Shackleton, J. (2011), "A comparative study of laser direct metal deposition characteristics using gas and plasma-atomized Ti-6Al-4V powders", *Materials Science and Engineering A*, Elsevier, Vol. 528 No. 25–26, pp. 7648–7657, doi: 10.1016/j.msea.2011.06.074.

Ali, H., Ghadbeigi, H. and Mumtaz, K. (2018), "Effect of scanning strategies on residual stress and mechanical properties of Selective Laser Melted Ti6Al4V", *Materials Science and Engineering A*, Elsevier, Vol. 712, pp. 175–187, doi: 10.1016/j.msea.2017.11.103.

Ali, H., Ma, L., Ghadbeigi, H. and Mumtaz, K. (2017), "In-situ residual stress reduction, martensitic decomposition and mechanical properties enhancement through high temperature powder bed pre-heating of Selective Laser Melted Ti6Al4V", *Materials Science and Engineering: A*, Elsevier, Vol. 695, pp. 211–220, doi: 10.1016/j.msea.2017.04.033.

AlMangour, B., Baek, M.S., Grzesiak, D. and Lee, K.A. (2018), "Strengthening of stainless steel by titanium carbide addition and grain refinement during selective laser melting", *Materials Science and Engineering A*, Elsevier, Vol. 712, pp. 812–818, doi: 10.1016/j.msea.2017.11.126.

AlMangour, B., Grzesiak, D. and Yang, J.M. (2017), "In-situ formation of novel TiC-particle-reinforced 316L stainless steel bulk-form composites by selective laser melting", *Journal of Alloys and Compounds*, Elsevier, Vol. 706, pp. 409–418, doi: 10.1016/j.jallcom.2017.01.149.

ASTM International. (2010), "Standard Specification for Titanium-6Aluminum-4Vanadium Alloy Castings for Surgical Implants (UNS R56406)", *Astm F1108-04*, doi: 10.1520/F1108-04R09.2.

Attar, H., Bönisch, M., Calin, M., Zhang, L.-C.C., Scudino, S. and Eckert, J. (2014), "Selective laser melting of in situ titanium-titanium boride composites: Processing, microstructure and mechanical properties", *Acta Materialia*, Pergamon, Vol. 76, pp. 13–22, doi: 10.1016/j.actamat.2014.05.022.

Attar, H., Bönisch, M., Calin, M., Zhang, L.C., Zhuravleva, K., Funk, A., Scudino, S., *et al.* (2014), "Comparative study of microstructures and mechanical properties of in situ Ti-TiB composites produced by selective laser melting, powder metallurgy, and casting

technologies", *Journal of Materials Research*, Vol. 29 No. 17, pp. 1941–1950, doi: 10.1557/jmr.2014.122.

Attar, H., Ehtemam-Haghighi, S., Kent, D. and Dargusch, M.S. (2018), "Recent developments and opportunities in additive manufacturing of titanium-based matrix composites: A review", *International Journal of Machine Tools and Manufacture*, Elsevier Ltd, Vol. 133 No. June, pp. 85–102, doi: 10.1016/j.ijmachtools.2018.06.003.

Bachmann, F., Hielscher, R. and Schaeben, H. (2010), "Texture analysis with MTEX- Free and open source software toolbox", *Solid State Phenomena*, Vol. 160, pp. 63–68, doi: 10.4028/www.scientific.net/SSP.160.63.

Bai, M., Namus, R., Xu, Y., Guan, D., Rainforth, M.W. and Inkson, B.J. (2019), "In-situ Ti-6Al-4V/TiC composites synthesized by reactive spark plasma sintering: processing, microstructure, and dry sliding wear behaviour", *Wear*, Elsevier, Vol. 432–433, p. 202944, doi: 10.1016/j.wear.2019.202944.

Bermingham, M.J., McDonald, S.D. and Dargusch, M.S. (2018), "Effect of trace lanthanum hexaboride and boron additions on microstructure, tensile properties and anisotropy of Ti-6Al-4V produced by additive manufacturing", *Materials Science and Engineering A*, Elsevier B.V., Vol. 719 No. December 2017, pp. 1–11, doi: 10.1016/j.msea.2018.02.012.

Cherry, J.A., Davies, H.M., Mehmood, S., Lavery, N.P., Brown, S.G.R. and Sienz, J. (2014), "Investigation into the effect of process parameters on microstructural and physical properties of 316L stainless steel parts by selective laser melting", *International Journal of Advanced Manufacturing Technology*, Vol. 76 No. 5–8, pp. 869–879, doi: 10.1007/s00170-014-6297-2.

Dadbakhsh, S., Mertens, R., Hao, L., Van Humbeeck, J. and Kruth, J. (2019), "Selective Laser Melting to Manufacture 'In Situ' Metal Matrix Composites: A Review", *Advanced Engineering Materials*, Vol. 21 No. 3, p. 1801244, doi: 10.1002/adem.201801244.

Dadbakhsh, S., Mertens, R., Vanmeensel, K., Ji, G. and Kruth, J.P. (2020), "In situ transformations during SLM of an ultra-strong TiC reinforced Ti composite", *Scientific Reports*, Nature Publishing Group UK, Vol. 10 No. 1, pp. 1–12, doi: 10.1038/s41598-020-67434-3.

DebRoy, T., Wei, H.L., Zuback, J.S., Mukherjee, T., Elmer, J.W., Milewski, J.O., Beese, A.M., *et al.* (2018), "Additive manufacturing of metallic components – Process, structure and properties", *Progress in Materials Science*, Pergamon, Vol. 92, pp. 112–224, doi: 10.1016/j.pmatsci.2017.10.001.

Donachie, M.J. (2000a), "A Primer on Titanium and Its Alloys", *Titanium: A Technical Guide*, Second., ASM International, Ohio, pp. 1–3, doi: 10.1361/tatg2000p001.

Donachie, M.J. (2000b), "Introduction to Selection of Titanium Alloys", *Titanium: A Technical Guide*, Second., ASM International, Ohio, pp. 5–11, doi: 10.1361/tatg2000p005.

Dunmead, S.D., Readey, D.W., Semler, C.E. and Hol, J.B. (1989), "Kinetics of Combustion Synthesis in the Ti-C and Ti-C-Ni Systems", *Journal of the American Ceramic Society*, Vol. 72 No. 12, pp. 2318–2324, doi: 10.1111/j.1151-2916.1989.tb06083.x.

Ferguson, J.B., Schultz, B.F., Venugopalan, D., Lopez, H.F., Rohatgi, P.K., Cho, K. and Kim, C.S. (2014), "On the superposition of strengthening mechanisms in dispersion strengthened alloys and metal-matrix nanocomposites: Considerations of stress and

energy", *Metals and Materials International*, Vol. 20 No. 2, pp. 375–388, doi: 10.1007/s12540-014-2017-6.

Freeman, F. (2018), *Structuring Difference The Additive Manufacture of Spatially & Functionally Differentiated Microstructures*, The University of Sheffield.

Gong, H., Rafi, K., Gu, H., Starr, T. and Stucker, B. (2014), "Analysis of defect generation in Ti-6Al-4V parts made using powder bed fusion additive manufacturing processes", *Additive Manufacturing*, Elsevier B.V., Vol. 1, pp. 87–98, doi: 10.1016/j.addma.2014.08.002.

Gu, D., Hagedorn, Y.C., Meiners, W., Wissenbach, K. and Poprawe, R. (2011a), "Selective Laser Melting of in-situ TiC/Ti5Si3 composites with novel reinforcement architecture and elevated performance", *Surface and Coatings Technology*, Elsevier B.V., Vol. 205 No. 10, pp. 3285–3292, doi: 10.1016/j.surfcoat.2010.11.051.

Gu, D., Hagedorn, Y.C., Meiners, W., Wissenbach, K. and Poprawe, R. (2011b), "Nanocrystalline TiC reinforced Ti matrix bulk-form nanocomposites by Selective Laser Melting (SLM): Densification, growth mechanism and wear behavior", *Composites Science and Technology*, Elsevier Ltd, Vol. 71 No. 13, pp. 1612–1620, doi: 10.1016/j.compscitech.2011.07.010.

Gu, D., Shen, Y. and Meng, G. (2009), "Growth morphologies and mechanisms of TiC grains during Selective Laser Melting of Ti-Al-C composite powder", *Materials Letters*, North-Holland, Vol. 63 No. 29, pp. 2536–2538, doi: 10.1016/j.matlet.2009.08.043.

Gu, D., Wang, H. and Zhang, G. (2014), "Selective laser melting additive manufacturing of Ti-based nanocomposites: The role of nanopowder", *Metallurgical and Materials Transactions A: Physical Metallurgy and Materials Science*, Vol. 45 No. 1, pp. 464–476, doi: 10.1007/s11661-013-1968-4.

Gu, D., Wang, Z., Shen, Y., Li, Q. and Li, Y. (2009), "In-situ TiC particle reinforced Ti-Al matrix composites: Powder preparation by mechanical alloying and Selective Laser Melting behavior", *Applied Surface Science*, North-Holland, Vol. 255 No. 22, pp. 9230–9240, doi: 10.1016/j.apsusc.2009.07.008.

Gu, D.D., Meiners, W., Wissenbach, K. and Poprawe, R. (2012), "Laser additive manufacturing of metallic components: materials, processes and mechanisms", *International Materials Reviews*, Vol. 57 No. 3, pp. 133–164, doi: 10.1179/1743280411Y.0000000014.

Günther, J., Krewerth, D., Lippmann, T., Leuders, S., Tröster, T., Weidner, A., Biermann, H., *et al.* (2017), "Fatigue life of additively manufactured Ti–6Al–4V in the very high cycle fatigue regime", *International Journal of Fatigue*, Vol. 94, pp. 236–245, doi: 10.1016/j.ijfatigue.2016.05.018.

Harrison, N.J., Todd, I. and Mumtaz, K. (2015), "Reduction of micro-cracking in nickel superalloys processed by Selective Laser Melting: A fundamental alloy design approach", *Acta Materialia*, Pergamon, Vol. 94, pp. 59–68, doi: 10.1016/J.ACTAMAT.2015.04.035.

He, Y., Montgomery, C., Beuth, J. and Webler, B. (2019), "Melt pool geometry and microstructure of Ti6Al4V with B additions processed by selective laser melting additive manufacturing", *Materials and Design*, Elsevier Ltd, Vol. 183, p. 108126, doi: 10.1016/j.matdes.2019.108126.

Hooper, P.A. (2018), "Melt pool temperature and cooling rates in laser powder bed fusion",

Additive Manufacturing, Elsevier, Vol. 22 No. May, pp. 548–559, doi: 10.1016/j.addma.2018.05.032.

Hu, Y., Cong, W., Wang, X., Li, Y., Ning, F. and Wang, H. (2018), "Laser deposition-additive manufacturing of TiB-Ti composites with novel three-dimensional quasi-continuous network microstructure: Effects on strengthening and toughening", *Composites Part B: Engineering*, Elsevier Ltd, Vol. 133, pp. 91–100, doi: 10.1016/j.compositesb.2017.09.019.

Huang, L.J., Geng, L. and Peng, H.X. (2011), "In situ TiBw/Ti composites with a novel quasi-continuous network reinforcement architecture", *ICCM International Conferences on Composite Materials*, pp. 1–5.

Kainer, K.U. (2006), "Basics of Metal Matrix Composites", *Metal Matrix Composites*, pp. 1–54, doi: doi:10.1002/3527608117.ch1.

Kasperovich, G., Haubrich, J., Gussone, J. and Requena, G. (2016), "Correlation between porosity and processing parameters in TiAl6V4 produced by selective laser melting", *Materials and Design*, Elsevier, Vol. 105, pp. 160–170, doi: 10.1016/j.matdes.2016.05.070.

Khairallah, S.A., Anderson, A.T., Rubenchik, A. and King, W.E. (2016), "Laser powder-bed fusion additive manufacturing: Physics of complex melt flow and formation mechanisms of pores, spatter, and denudation zones", *Acta Materialia*, Elsevier Ltd, Vol. 108, pp. 36–45, doi: 10.1016/j.actamat.2016.02.014.

Kim, I.Y., Choi, B.J., Kim, Y.J. and Lee, Y.Z. (2011), "Friction and wear behavior of titanium matrix (TiB+TiC) composites", *Wear*, Elsevier, Vol. 271 No. 9–10, pp. 1962–1965, doi: 10.1016/j.wear.2010.12.072.

Kondoh, K. (2015), "Titanium metal matrix composites by powder metallurgy (PM) routes", *Titanium Powder Metallurgy : Science, Technology and Applications*, Elsevier, pp. 277–297, doi: 10.1016/B978-0-12-800054-0.00016-2.

Kühnle, T. and Partes, K. (2012), "In-Situ Formation of Titanium Boride and Titanium Carbide by Selective Laser Melting", *Physics Procedia*, Vol. 39, pp. 432–438, doi: 10.1016/j.phpro.2012.10.058.

Kun, C., Beibei, H., Wenheng, W. and Cailin, Z. (2017), "The formation mechanism of TiC reinforcement and improved tensile strength in additive manufactured Ti matrix nanocomposite", *Vacuum*, Pergamon, Vol. 143, pp. 23–27, doi: 10.1016/j.vacuum.2017.05.029.

Liu, S. and Shin, Y.C. (2017), "The influences of melting degree of TiC reinforcements on microstructure and mechanical properties of laser direct deposited Ti6Al4V-TiC composites", *Materials and Design*, Elsevier Ltd, Vol. 136, pp. 185–195, doi: 10.1016/j.matdes.2017.09.063.

Ma, C., Zhao, J., Cao, C., Lin, T.-C. and Li, X. (2016), "Fundamental Study on Laser Interactions With Nanoparticles-Reinforced Metals—Part II: Effect of Nanoparticles on Surface Tension, Viscosity, and Laser Melting", *Journal of Manufacturing Science and Engineering*, Vol. 138 No. 12, pp. 2–7, doi: 10.1115/1.4033446.

Ma, F., Zhou, J., Liu, P., Li, W., Liu, X., Pan, D., Lu, W., *et al.* (2017), "Strengthening effects of TiC particles and microstructure refinement in in situ TiC-reinforced Ti matrix composites", *Materials Characterization*, Elsevier Inc., Vol. 127, pp. 27–34, doi:

10.1016/j.matchar.2017.02.004.

Manvatkar, V., De, A. and DebRoy, T. (2015), "Spatial variation of melt pool geometry, peak temperature and solidification parameters during laser assisted additive manufacturing process", *Materials Science and Technology (United Kingdom)*, Vol. 31 No. 8, pp. 924–930, doi: 10.1179/1743284714Y.0000000701.

Montgomery, D.C. (2017), "Response Surface Methods and Designs", *Design and Analysis of Experiments*, 9th ed., John Wiley & Sons, Inc., pp. 489–568.

Niessen, F., Nyyssönen, T., Gazder, A.A. and Hielscher, R. (2021), "Parent grain reconstruction from partially or fully transformed microstructures in MTEX", *Journal of Chemical Information and Modeling*, Vol. 53 No. 9, pp. 1689–1699, doi: 10.1088/1751-8113/44/8/085201.

Okamoto, H. (2006), "C−Ti (Carbon-Titanium)", *Journal of Phase Equilibria and Diffusion*, Vol. 27 No. 3, pp. 306–307, doi: 10.1361/154770306x109980.

Pan, S., Zhou, X., Chen, K., Yang, M., Cao, Y., Chen, X. and Wang, Z. (2018), "In-situ nanoparticles: A new strengthening method for metallic structural material", *Applied Sciences (Switzerland)*, Vol. 8 No. 12, doi: 10.3390/app8122479.

Patil, A.S., Hiwarkar, V.D., Verma, P.K. and Khatirkar, R.K. (2019), "Effect of TiB2 addition on the microstructure and wear resistance of Ti-6Al-4V alloy fabricated through direct metal laser sintering (DMLS)", *Journal of Alloys and Compounds*, Elsevier B.V, Vol. 777, pp. 165–173, doi: 10.1016/j.jallcom.2018.10.308.

Peters, M., Hemptenmacher, J., Kumpfert, J. and Leyens, C. (2005), "Structure and Properties of Titanium and Titanium Alloys", *Titanium and Titanium Alloys*, Wiley-VCH Verlag GmbH & Co. KGaA, Weinheim, FRG, pp. 1–36, doi: 10.1002/3527602119.ch1.

Qiu, C., Panwisawas, C., Ward, M., Basoalto, H.C., Brooks, J.W. and Attallah, M.M. (2015), "On the role of melt flow into the surface structure and porosity development during selective laser melting", *Acta Materialia*, Pergamon, Vol. 96, pp. 72–79, doi: 10.1016/j.actamat.2015.06.004.

Rielli, V. V., Amigó-Borrás, V. and Contieri, R.J. (2019), "Microstructural evolution and mechanical properties of in-situ as-cast beta titanium matrix composites", *Journal of Alloys and Compounds*, Vol. 778, pp. 186–196, doi: 10.1016/j.jallcom.2018.11.093.

Sames, W.J., List, F.A., Pannala, S., Dehoff, R.R. and Babu, S.S. (2016), "The metallurgy and processing science of metal additive manufacturing", *International Materials Reviews*, Vol. 61 No. 5, pp. 315–360, doi: 10.1080/09506608.2015.1116649.

Schindelin, J., Arganda-Carreras, I., Frise, E., Kaynig, V., Longair, M., Pietzsch, T., Preibisch, S., *et al.* (2012), "Fiji: an open-source platform for biological-image analysis", *Nature Methods*, Vol. 9 No. 7, pp. 676–682, doi: 10.1038/nmeth.2019.

Shipley, H., McDonnell, D., Culleton, M., Coull, R., Lupoi, R., O'Donnell, G. and Trimble, D. (2018), "Optimisation of process parameters to address fundamental challenges during selective laser melting of Ti-6Al-4V: A review", *International Journal of Machine Tools and Manufacture*, Pergamon, Vol. 128, pp. 1–20, doi: 10.1016/j.ijmachtools.2018.01.003.

Simonelli, M., Tse, Y.Y. and Tuck, C. (2014a), "On the texture formation of selective laser melted Ti-6Al-4V", *Metallurgical and Materials Transactions A: Physical Metallurgy and Materials Science*, Vol. 45 No. 6, pp. 2863–2872, doi: 10.1007/s11661-014-2218-0.

Simonelli, M., Tse, Y.Y. and Tuck, C. (2014b), "Effect of the build orientation on the mechanical properties and fracture modes of SLM Ti-6Al-4V", *Materials Science and Engineering A*, Elsevier, Vol. 616, pp. 1–11, doi: 10.1016/j.msea.2014.07.086.

Storms, E.K.B.T.-R.M. (Ed.). (1967), "I - The Titanium–Titanium Carbide System", *The Refractory Carbides*, Vol. 2, Elsevier, pp. 1–17, doi: https://doi.org/10.1016/B978-1-4832-3070-2.50006-9.

Sun, X., Han, Y., Cao, S., Qiu, P. and Lu, W. (2017), "Rapid in-situ reaction synthesis of novel TiC and carbon nanotubes reinforced titanium matrix composites", *Journal of Materials Science and Technology*, The Society of Manufacturing Engineers, Vol. 33 No. 10, pp. 1165–1171, doi: 10.1016/j.jmst.2017.07.005.

Tjong, S.C. and Ma, Z.Y. (2000), "Microstructural and mechanical characteristics of in situ metal matrix composites", *Materials Science and Engineering: R: Reports*, Vol. 29 No. 3–4, pp. 49–113, doi: 10.1016/S0927-796X(00)00024-3.

Vilaro, T., Colin, C. and Bartout, J.D. (2011), "As-fabricated and heat-treated microstructures of the Ti-6Al-4V alloy processed by selective laser melting", *Metallurgical and Materials Transactions A: Physical Metallurgy and Materials Science*, Vol. 42 No. 10, pp. 3190–3199, doi: 10.1007/s11661-011-0731-y.

Vrancken, B., Dadbakhsh, S., Mertens, R., Vanmeensel, K., Vleugels, J., Yang, S. and Kruth, J.P. (2019), "Selective Laser Melting process optimization of Ti–Mo–TiC metal matrix composites", *CIRP Annals*, CIRP, Vol. 68 No. 1, pp. 221–224, doi: 10.1016/j.cirp.2019.04.120.

Wang, J., Li, L., Lin, P. and Wang, J. (2018), "Effect of TiC particle size on the microstructure and tensile properties of TiCp/Ti6Al4V composites fabricated by laser melting deposition", *Optics & Laser Technology*, Elsevier Ltd, Vol. 105, pp. 195–206, doi: 10.1016/j.optlastec.2018.03.009.

Wei, W.-H., Shao, Z.-N., Shen, J. and Duan, X.-M. (2017), "Microstructure and mechanical properties of in situ formed TiC-reinforced Ti–6Al–4V matrix composites", *Materials Science and Technology*, Vol. 0836, pp. 1–8, doi: 10.1080/02670836.2017.1366737.

Yu, W.H., Sing, S.L., Chua, C.K., Kuo, C.N. and Tian, X.L. (2019), "Particle-reinforced metal matrix nanocomposites fabricated by selective laser melting: A state of the art review", *Progress in Materials Science*, Pergamon, Vol. 104, pp. 330–379, doi: 10.1016/j.pmatsci.2019.04.006.

Yuan, P., Gu, D. and Dai, D. (2015), "Particulate migration behavior and its mechanism during selective laser melting of TiC reinforced Al matrix nanocomposites", *Materials and Design*, Elsevier Ltd, Vol. 82, pp. 46–55, doi: 10.1016/j.matdes.2015.05.041.

Zhang, K., Tian, X., Bermingham, M., Rao, J., Jia, Q., Zhu, Y., Wu, X., *et al.* (2019), "Effects of boron addition on microstructures and mechanical properties of Ti-6Al-4V manufactured by direct laser deposition", *Materials and Design*, Vol. 184, doi: 10.1016/j.matdes.2019.108191.

Zhang, L.C. and Attar, H. (2016), "Selective Laser Melting of Titanium Alloys and Titanium Matrix Composites for Biomedical Applications: A Review", *Advanced Engineering Materials*, Vol. 18 No. 4, pp. 463–475, doi: 10.1002/adem.201500419.